Bone 181 (2024) 117024

Contents lists available at ScienceDirect

Bone

journal homepage: www.elsevier.com/locate/bone

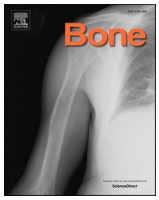

Full Length Article

Adaptive enhancement of apatite crystal orientation and Young's modulus under elevated load in rat ulnar cortical bone

Jun Wang [a,b,1], Takuya Ishimoto [a,c,1], Tadaaki Matsuzaka [a,1], Aira Matsugaki [a], Ryosuke Ozasa [a], Takuya Matsumoto [d], Mikako Hayashi [e], Hyoung Seop Kim [f], Takayoshi Nakano [a,*]

[a] Division of Materials and Manufacturing Science, Graduate School of Engineering, Osaka University, 2-1 Yamadaoka, Suita, Osaka 565-0871, Japan
[b] Division of Material Science and Engineering, Zhengzhou University, 100 Science Avenue, Zhengzhou, Henan 450001, China
[c] Aluminium Research Center, University of Toyama, 3190 Gofuku, Toyama 930-8555, Japan
[d] Department of Biomaterials, Graduate School of Medicine, Dentistry and Pharmaceutical Sciences, Okayama University, 2-5-1, Shikata-cho, Kita-ku, Okayama 700-8558, Japan
[e] Department of Restorative Dentistry and Endodontology, Graduate School of Dentistry, Osaka University, 1-8 Yamadaoka, Suita, Osaka 565-0871, Japan
[f] Department of Materials Science and Engineering, Pohang University of Science and Technology, Pohang 37673, South Korea

ARTICLE INFO

Keywords:
Functional adaptation
Bone strength
Apatite orientation
Bone quality
In vivo loading

ABSTRACT

Functional adaptation refers to the active modification of bone structure according to the mechanical loads applied daily to maintain its mechanical integrity and adapt to the environment. Functional adaptation relates to bone mass, bone mineral density (BMD), and bone morphology (*e.g.*, trabecular bone architecture). In this study, we discovered for the first time that another form of bone functional adaptation of a cortical bone involves a change in bone quality determined by the preferential orientation of apatite nano-crystallite, a key component of the bone. An *in vivo* rat ulnar axial loading model was adopted, to which a 3–15 N compressive load was applied, resulting in approximately 440–3200 με of compression in the bone surface. In the loaded ulnae, the degree of preferential apatite *c*-axis orientation along the ulnar long axis increased in a dose-dependent manner up to 13 N, whereas the increase in BMD was not dose-dependent. The Young's modulus along the same direction was enhanced as a function of the degree of apatite orientation. This finding indicates that bone has a mechanism that modifies the directionality (anisotropy) of its microstructure, strengthening itself specifically in the loaded direction. BMD, a scalar quantity, does not allow for load-direction-specific strengthening. Functional adaptation through changes in apatite orientation is an excellent strategy for bones to efficiently change their strength in response to external loading, which is mostly anisotropic.

1. Introduction

Bone structure is partly regulated by mechanical forces applied to the bone during daily physical activities. Roux and Wolff have previously recognized the functional adaptation of the bone to increased mechanical loading and the relationship between mechanical loading and bone structure [1]. Rubin and Lanyon have reported on the existence of a minimum strain threshold for this phenomenon, such that the applied loads that produce strains below this threshold induce no change in bone formation. In contrast, loads above this threshold increase bone formation in a dose-dependent manner [2]. Frost further articulated the importance of functional bone strain as a controlling stimulus for bone architecture, a relationship currently known as the mechanostat [3]. To date, numerous studies have been conducted on the functional adaptation of a cortical bone, most of which have focused on bone formation and resorption, *i.e.*, increases or decreases in bone mass. Adaptive changes in bone microstructural anisotropy, such as the preferential orientation of the biological apatite *c*-axis/collagen under increased mechanical loading, remain unclear.

Apatite has a hexagonal crystal structure (Supplementary Fig. 1S)

* Corresponding author at: Division of Materials and Manufacturing Science, Graduate School of Engineering, Osaka University, 2-1, Yamadaoka, Suita, Osaka 565-0871, Japan.
E-mail addresses: wangj@zzu.edu.cn (J. Wang), ishimoto@sus.u-toyama.ac.jp (T. Ishimoto), tadaaki.matsuzaka@mat.eng.osaka-u.ac.jp (T. Matsuzaka), matsugaki@mat.eng.osaka-u.ac.jp (A. Matsugaki), ozasa@mat.eng.osaka-u.ac.jp (R. Ozasa), tmatsu@md.okayama-u.ac.jp (T. Matsumoto), hayashi.mikako.dent@osaka-u.ac.jp (M. Hayashi), hskim@postech.ac.kr (H.S. Kim), nakano@mat.eng.osaka-u.ac.jp (T. Nakano).
[1] These authors contributed equally.

https://doi.org/10.1016/j.bone.2024.117024
Received 9 November 2023; Received in revised form 2 January 2024; Accepted 19 January 2024
Available online 23 January 2024

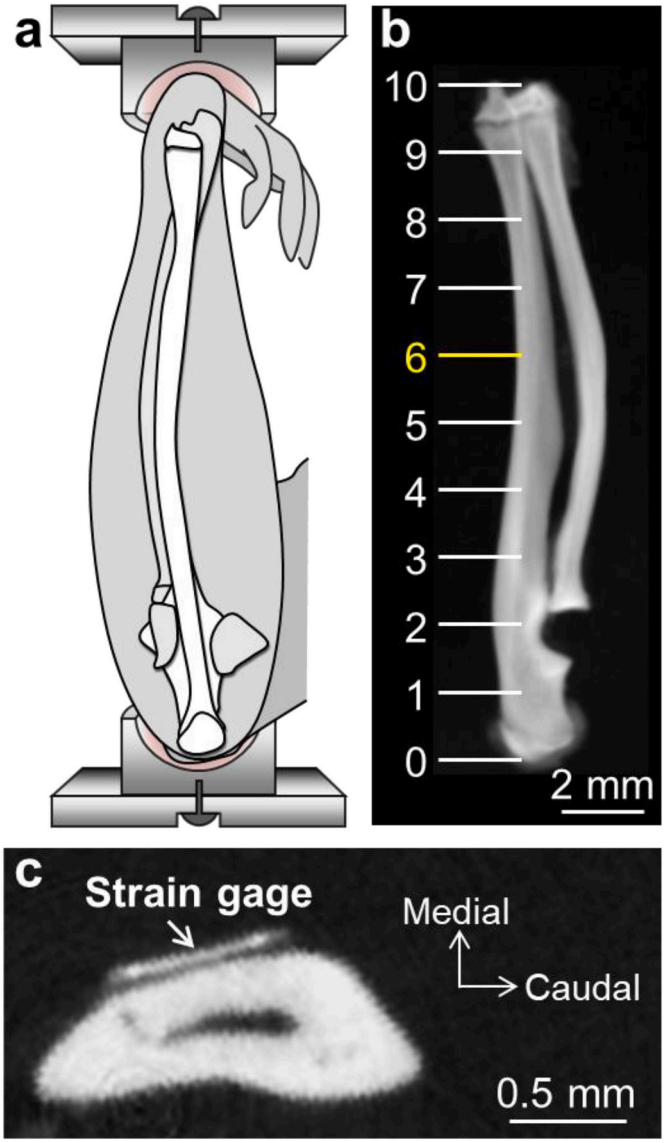

Fig. 1. Description of *in vivo* rat ulnar loading model. (a) Schematic of *in vivo* rat ulnar loading model, (b) definition of bone portion, and (c) cross-sectional image at Point 6 with strain gauge on the medial surface.

and shows anisotropy in Young's modulus; the modulus is higher along the *c*-axis compared to the *a*-axis [4]. Collagen molecules form fibers, which exhibit higher strength in the fiber direction [5]. Based on such anisotropy at the molecular level, bones as aggregates exhibit anisotropic mechanical properties such as Young's modulus [6,7], yield stress [6], and toughness [8,9] based on their orientation condition. Since bones have a hierarchical anisotropy in structure ranging from molecular scale to macroscopic shape [10], the form of anisotropic arrangements at each scale level is believed to govern the mechanical properties and their anisotropy of bones. We have been using microbeam X-ray diffraction (μXRD) to evaluate apatite orientation as average information within a region with ~100 μm length scale encompassing the multiple lamellar structures. The positive correlation between the degree of apatite *c*-axis orientation and the local Young's modulus obtained in the same region was reported [11]. Therefore, considering anisotropic microorganization is important to understand bone mechanobiology, including the adaptive response of the bone to the mechanical environment. According to a previous study [12], the apatite/collagen orientation is consistent with the principal *in vivo* stress direction and varies depending on the bone type, shape, and anatomical location in the body; the apatite/collagen orientation may be modified in response to *in vivo* stress conditions. To the best of our knowledge, no previous studies have addressed the relationship between apatite/collagen orientation and the elevated strain environment. We hypothesized that cortical bone changes its anisotropic microarrangement of the apatite *c*-axis and collagen to make the bone material mechanically anisotropic along the principally loaded direction under the mechanical environment, which is thought to be a more effective strategy for bone strength adaptation to the altered load. We used an *in vivo* rat ulnar loading model, which is well accepted as a non-destructive animal model for investigating the adaptive response of the cortical bone [13–15], to elucidate the adaptive bone responses by altering the preferential apatite orientation and determining the functional strain range.

2. Materials and methods

2.1. Animals

In vivo loading experiments were performed to clarify the adaptive bone responses to elevated loads in rats. Since rats do not undergo intracortical remodeling, it was assumed that, at an elevated load, bone would be added to the bone surface. The amount of bone added in long bones decreases monotonically with increasing age (*e.g.*, approximately 9–10, 5–6, and 2 μm/day at 4, 8, and 16 weeks of age in the femur and tibia, respectively) [16]. Eight-week-old rats were used for the analysis to ensure sufficient periosteal bone formation.

Forty-five male Sprague-Dawley rats (age: 7 weeks; body weight: 200 g) were purchased from Japan SLC (Shizuoka, Japan). The animals were individually housed in a cage with a 12:12 h light: dark cycle. They were provided with a standard diet (CRF-1; Oriental Yeast, Tokyo, Japan) and tap water *ad libitum* and acclimated for one week before experimentation. At eight weeks of age, three rats were used to determine the relationship between mechanical strain on the ulna and the applied load. Twelve rats were used for the *in vivo* loading experiment to analyze bone apposition and microdamage formation for two weeks. The remaining thirty rats were used for the *in vivo* loading experiment for eight weeks to analyze the adaptive changes in bone mass, BMD, apatite orientation, and Young's modulus to elevated load. The overall experimental design is shown in Supplementary Fig. 2S. All procedures were approved by the Animal Experiment Committee of Osaka University Graduate School of Engineering (approval number: 22-1-0). Before and after the loading, the rats were allowed unrestricted cage activity.

2.2. In vivo ulnar loading model and bone site for analyses

In vivo ulnar loading was performed as previously described (Fig. 1a) [13–15] under anesthesia (pentobarbital sodium; Dainippon Sumitomo Pharma, Osaka, Japan). The anesthetized rats were placed on a mat, and the right forelimb was held in rounded cups between the olecranon process of the ulna and the flexed carpus. The right forelimb was cyclically loaded in the compression mode with a peak compression load of 3, 5, 7, 10, 13, and 15 N at 2 Hz for 1200 cycles/day, five days/week, using a micro-material testing machine (MMT-101 N; Shimadzu, Kyoto, Japan) (loaded group). The load frequency of 2 Hz corresponds to the stride frequency during natural locomotion [17,18]. The left forelimb received no treatment, considering it was the control (CTL) group.

Adaptive bone formation in the ulna under an elevated load is site-specific and depends on the magnitude of the locally generated strain [19]. According to previous reports, the magnitude of the generated strain owing to the *in vivo* loading and the amount of bone formation peaked at the medial surface, approximately 3–4 mm distal to the ulnar midshaft [19–21]. Therefore, in this study, the analyses were performed at comparable locations on the ulna (Point 6, as shown in Fig. 1b), according to these studies.

2.3. Load-strain relationship measurements

Three animals were used to establish an artificial load-strain relationship. Following anesthesia, the medial surface of the right ulna at Point 6 was minimally exposed. The periosteum and any attached tissue were gently removed. The medial surface was cleaned with 70 % ethanol and dried, and a single-element strain gauge (KFRS-020120-C1-13L1M3R; Kyowa Electronic Instruments, Tokyo, Japan) was bonded longitudinally on this area with a cyanoacrylate adhesive (CC-33A, Kyowa Electronic Instruments) (Fig. 1c). Gentle pressure for 1 min facilitated a strong attachment of the gauge to the bone surface. The incision was then sutured. The forearm was axially loaded for each peak load to be investigated in the order of 3, 5, 7, 10, 13, and 15 N, followed by 3 N at a frequency of 2 Hz for approximately ten cycles; the generated strain was recorded using a sensor interface (PCD-300B, Kyowa Electronic Instruments). The magnitude of the generated strain recorded in the second exposure to 3 N was not reduced, suggesting that no damage was induced during series of loading; therefore, the obtained strains were valid. This loading regimen allowed us to create a dose-response relationship between load magnitude and strain.

2.4. In vivo ulnar loading

Thirty rats were randomly divided into six groups ($n = 5$) for the *in vivo* loading experiment with each load, and the right forelimb of each animal was subjected to 1200 loading cycles (10 min) per day at a frequency of 2 Hz, five days/week for eight weeks. The left forelimbs were not loaded and served as controls. All rats were euthanized on Day 56 using an overdose of pentobarbital sodium, and the ulnae and radii were immediately removed and immersed in a 10 % formalin-neutral buffered solution for chemical fixation.

2.5. Assessment of bone length by radiography

Soft X-ray photographs were taken after removing the ulnae using XIE (Chubu Medical, Mie, Japan) at 40 kV, 40 μA and 71 msec radiation. An antero-posterior projection was performed, and the ulnar length was measured to determine the analytical portion (Point 6).

2.6. Assessment of bone formation in response to elevated loading

To assess bone formation in response to elevated load and microdamage, 12 rats were loaded with each load for 1200 cycles/day for two weeks. Calcein (Dojindo, Kumamoto, Japan) was administered intraperitoneally at a dose rate of 8 mg/kg before the onset of the loading experiment (Day 1) and on Day 15. On Day 18, all animals were euthanized, and the ulnae were harvested and stored in 70 % ethanol overnight. Bones were stained *en bloc* with basic fuchsin (Wako, Osaka, Japan) to stain the induced microdamage using an established protocol [22]. Following staining, the bones were rinsed in 100 % ethanol, followed by 100 % Clear-Rite 3 (Richard-Allen Scientific, MI, USA) for 12 h under vacuum, and then embedded in methyl methacrylate (Mager Scientific, MI, USA). Serial cross-sections of 1 mm thickness were cut using a diamond saw (BS-300CP; Exakt Apparatebau, Norderstedt, Germany). The sections were ground using emery paper (800, 1200, and 2000 grids) to a final thickness of approximately 500 μm.

Confocal laser scanning microscopy (CLSM) (FV1000D-IX81; Olympus, Tokyo, Japan) was used to examine the bone sections stained with calcein and fuchsin dyes. Two-dimensional images were taken from near the section surface. Fluorescence images showing calcein labelling were captured using a UPlanSApo 10× (numerical aperture = 0.4) magnification objective lens and 488 nm excitation to utilize the fluorescence of calcein and eliminate background autofluorescence of the bone. Basic fuchsin also acts as an excellent fluorochrome and fluoresces strongly at 585 nm under 568 nm excitation. Microcracks or microdamages stained with basic fuchsin were visualized using CLSM with a UPlanSApo60× (numerical aperture = 1.35) magnification oil immersion objective lens. A single researcher performed all imaging and analyses under non-blinded conditions. The same applies hereafter.

2.7. Assessment of bone area and geometry using microfocus X-ray CT

For the removed bone, CT images were obtained using a microfocus X-ray CT (SMX-100CT; Shimadzu, Kyoto, Japan) under 70 kV and 80 μA radiation with a spatial resolution of 19.53 μm. To ensure sufficient spatial resolution for quantitative evaluation, the Point 6 area was enlarged and photographed. After the CT images were binarized, the cortical bone area (mm^2) and second moment of inertia (I) (mm^4) with a neutral axis were assumed to be along the mediolateral and craniocaudal directions ($I_{M\text{-}L}$ and $I_{C\text{-}C}$, respectively) and calculated using 3D image analysis software (Tri/3D-BON, Ratoc System Engineering, Tokyo, Japan). For each individual animal, the relative ratio of the second moment of inertia in the artificially loaded group to the CTL group was calculated.

2.8. Assessment of BMD by peripheral quantitative computed tomography (pQCT)

Volumetric BMD (mg/cm^3) was measured using pQCT (XCT Research SA+; Stratec Medizintechnik, Birkenfeld, Germany). The ulna was placed in a plastic tube filled with 10 % formalin. After performing a scout view to enable scan localization, a cross-sectional scan was performed using a 70 × 70 × 460 μm resolution. The data for each pixel (70 × 70 μm) was exported in ASCII format into Microsoft Excel software. The bone cross-section at the end of the eight-week experiment (16 weeks old) was overlaid on the bone cross-section at the onset of the study (eight weeks old), using the small marrow cavity as a landmark to identify the bone areas that had formed during the eight-week experimental period (Supplementary Fig. 3S). The BMD of the bone region newly formed during the experimental period was calculated in an area of 70 × 350 μm near the medial surface. The cortical bone was judged to be above a threshold value of 690 mg/cm^3. The BMD values were calibrated using phantoms.

2.9. Assessment of preferential orientation of the apatite c-axis (bone quality) using μXRD

The degree of apatite *c*-axis orientation as a bone quality parameter was analyzed using a μXRD system (R-axis BQ, Rigaku, Tokyo, Japan) equipped with a transmission-type optical system and an imaging plate (storage phosphors) (Fujifilm, Tokyo, Japan) placed behind the specimen. The crystallographic *c*-axis of apatite aligns almost parallel to the collagen fiber direction because of an epitaxial crystallization of apatite on the collagen template; therefore, the degree of apatite *c*-axis orientation reflects that of collagen fiber [23]. Mo-Kα radiation with a wavelength of 0.07107 nm was generated at a tube voltage of 50 kV and a tube current of 90 mA. The incident beam was focused on a beam spot of 100 μm in diameter by a double-pinhole metal collimator and radiated along the mediolateral axis, grazing the medial bone surface such that half of the incident beam passed through the bone specimen (Supplementary Fig. 4S) [24]. In this case, diffraction information from the bone tissue within 50 μm of the cranial bone surface alone was collected to determine the degree of apatite orientation solely in the newly formed bone owing to *in vivo* artificial loading. Diffraction data were collected for 900 s. The measurement was performed on the medial surface of the distal ulnae diaphysis (Point 6), at which new bone formation peaked (see Results).

From the obtained diffraction intensity pattern (Debye ring), the degree of preferential orientation of apatite *c*-axis was determined as the relative intensity ratio of two representative diffraction peaks for apatite, (002) and (310) [11,25]. The apatite *c*-axis preferentially orients along the longitudinal axis of long bones [11,25]. Therefore, in this

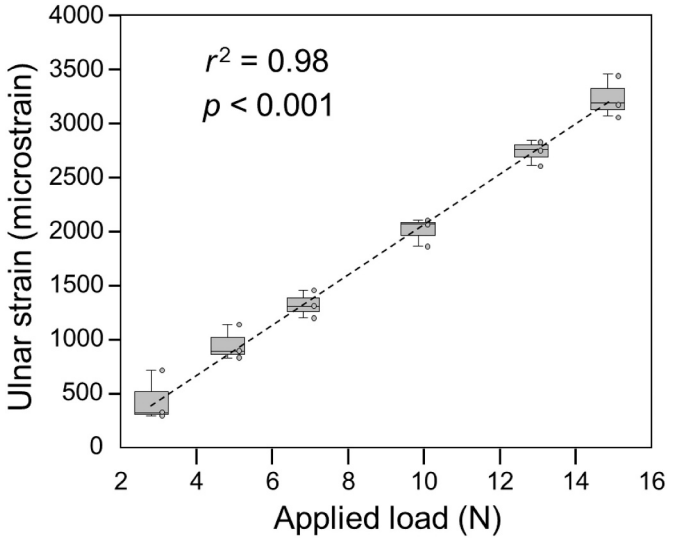

Fig. 2. Artificial loading-induced compressive strain along the ulnar long axis on the medial surface at point 6. Data are displayed in a box-and-whisker diagram. $n = 3$.

study, the diffracted information along the long axis of the ulna was analyzed (Supplementary Fig. 4S). The upper and lower parts of the Debye ring corresponded with the long axes of the ulnae. The diffraction intensities were azimuthally integrated in the range of 100 pixels to obtain an X-ray diffraction profile. The degree of preferential orientation of the *c*-axis in the apatite crystals was determined from the relative intensity ratio of the (002) diffraction peak to the (310) peak in the X-ray profile. The intensity ratios calculated for the upper and lower parts of the Debye ring were averaged. Randomly oriented hydroxyapatite (NIST #2910: calcium hydroxyapatite) powder had an intensity ratio of 0.8; therefore, detected values >0.8 indicated the presence of anisotropic apatite *c*-axis orientation in the analyzed direction.

2.10. Analysis of Young's modulus by nanoindentation

After the samples were dried, Young's modulus was measured along the ulnar longitudinal direction using a nanoindentation system (ENT-1100a; Elionix, Tokyo, Japan) with a Berkovich diamond indenter at 25 °C, as described in a previous study [26]. Five indentations were created on the medial region within 50 μm from the periosteal surface, in which the μXRD analysis was performed, and the results were averaged. The loading/unloading rate and maximum load were 400 μN/s and 6000 μN, respectively. A constant maximum load was held for 180 s before unloading to minimize the effects of the viscoelastic behavior of bone [26]. All measurements included a second constant load held for 30 s at 10 % of the maximum load to establish the thermal drift rate and obtain the correct data. Young's modulus was determined using the method described by Oliver and Pharr [27]. BMD, apatite orientation, and Young's modulus were analyzed under the most similar region and dimension conditions possible.

2.11. Statistical analyses

Quantitative data are presented as mean ± standard deviation in the text and box-and-whisker plots in the figures. For the data comparison between the CTL and loaded groups, a two-tailed paired *t*-test was used. The significance of load magnitude-dependent changes was tested using a one-way analysis of variance (ANOVA). A Tukey's *post hoc* significant difference (HSD) multiple comparison test was conducted. Pearson's correlation and multiple linear regression analyses were used to establish the significant determinants of Young's modulus. The BMD and degree of apatite *c*-axis orientation were considered independent variables in multiple linear regression analysis. A multiple regression coefficient (β) was used to identify the dominant determinant. $p < 0.05$ was considered statistically significant.

3. Results

During the loading experiment, three 15 N-loaded ulnae fractured in the first and second weeks. Data for the remaining two 15 N-loaded animals will be presented but excluded from the statistical analyses.

3.1. In vivo load-strain relationship

The relationship between the applied load and strain at the distal ulnar diaphyseal surface (point 6) is shown in Fig. 2. The strain values due to loading at 3, 5, 7, 10, 13, and 15 N were determined to be 442 ± 232 με, 947 ± 162 με, 1310 ± 127 με, 2000 ± 128 με, 2708 ± 114 με, and 3200 ± 197 με, respectively. Thus, we obtained the relation between the ulnar strain and peak load, which represented a highly significant ($p < 0.001$) linear regression with $r^2 = 0.98$.

3.2. Bone formation in response to artificial loading

Fig. 3a–e shows the double-labeled calcein ulnar cross-section representing new bone formed during the experiment at the distal diaphysis

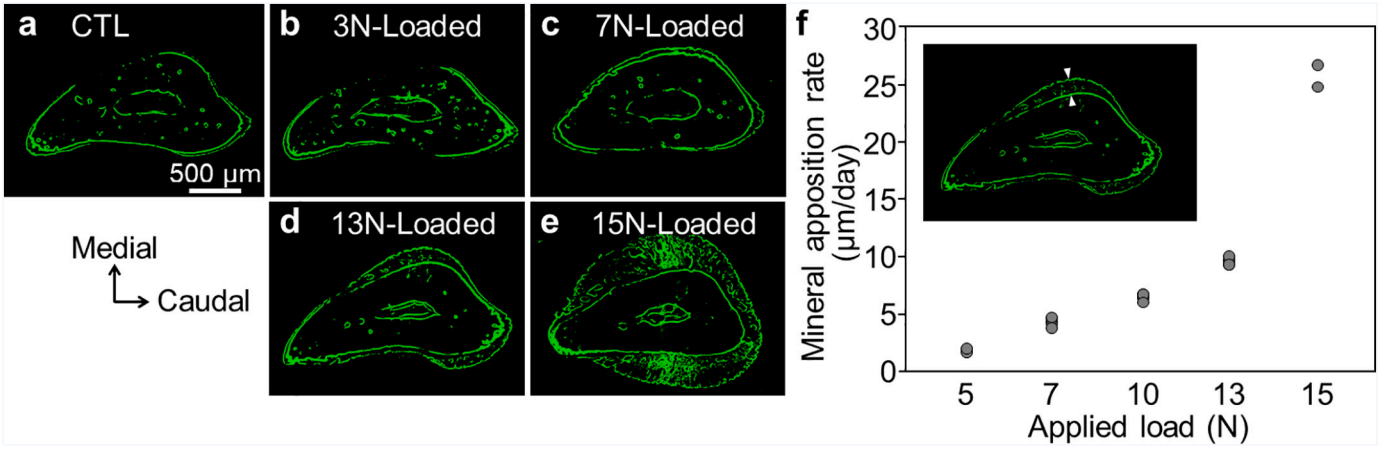

Fig. 3. Bone formation induced by artificial loading. (a–e) Confocal fluorescence images of cross-sections at Point 6 showing calcein labeling. (f) Change in mineral apposition rate at the medial periosteum as a function of applied artificial load determined by the distance between the first (inner) and second (outer) labeling. $n = 2$.

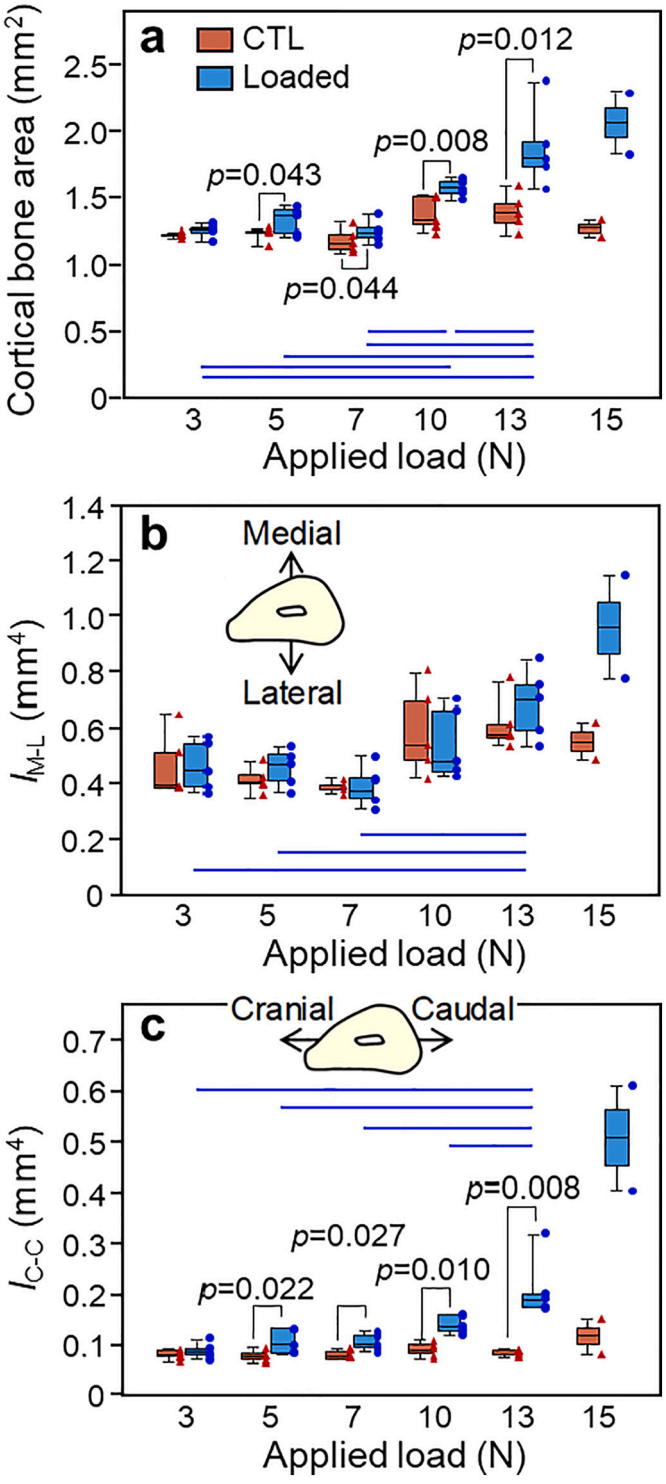

Fig. 4. Artificial loading-related change in bone mass. Change in (a) cortical bone area, (b) second moment of inertia (I) with respect to the medio-lateral (M-L) axis, and (c) that with respect to the cranio-caudal (C-C) axis, measured at Point 6 after loading for eight weeks. Quantitative data is displayed in a box-and-whisker diagram. Horizontal bars indicate significant differences in Tukey's HSD test.

(Point 6). In the CTL group, after two weeks of normal growth, the medial ulnar periosteal surfaces showed clear evidence of bone resorption, with no continuous fluorochrome incorporation (Fig. 3a). In contrast, in the equivalent regions of the loaded ulnae, except for the 3 N-loaded bones (Fig. 3b), continuous incorporation of the second

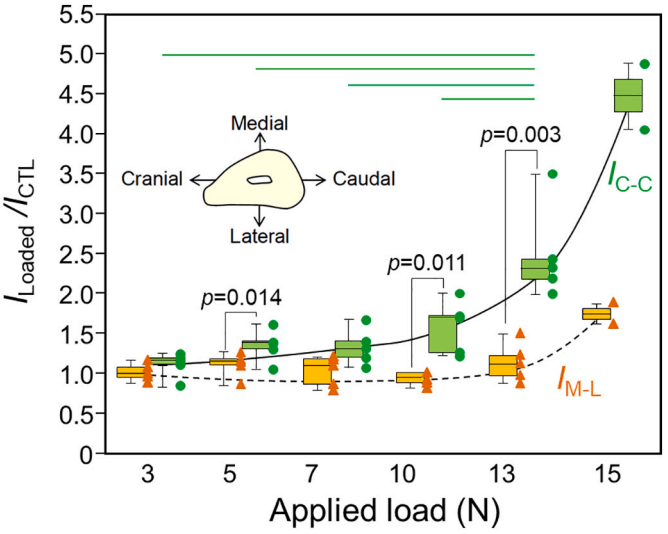

Fig. 5. Relative ratio of the second moment of inertia in the artificially loaded group to the CTL group. $I_{M\text{-}L}$: the second moment of inertia with respect to the medio-lateral (M-L) axis; $I_{C\text{-}C}$: the second moment of inertia with respect to the cranio-caudal (C-C) axis. Data are displayed in a box-and-whisker diagram. The horizontal bar indicates significant differences in Tukey's HSD test. $n = 5$ for 5–13 N, and $n = 2$ for 15 N.

fluorochrome label was observed, clearly indicating loading-induced bone formation at the medial periosteal surface (Fig. 3c–e). Fig. 3f shows the mineral apposition rate on the medial periosteal surface as a function of the applied load, calculated from the confocal fluorescence images. Because of the absence of double labeling, the 3 N load group was not used for this analysis. The mineral apposition rate in the loaded bone gradually increased as the applied load increased. With 13 N loading, the mineral apposition rate reached almost 10 μm/day, which is approximately twice the reported apposition rate in the long bone diaphysis of rats at eight weeks of age [16]. In the 15 N-loaded group, a drastic increase in the mineral apposition rate was observed, and the newly formed bone under an artificial load was woven (Fig. 3e).

3.3. *Effect of load magnitude on bone area and geometry*

Fig. 4a shows the change in cortical bone area after the *in vivo* loading experiment. No discernible responses were observed in the 3 N group. In the 5–13 N groups, the cross-sectional area of the ulnae subjected to loading increased significantly with increasing load magnitude ($p < 0.001$ by one-way ANOVA). With 13 N loading, the bone area increased approximately 1.3-fold compared to the CTL group.

Fig. 4b and c show the loading-related change in the second moment of inertia, which reflects the bone structure's resistance to bending by considering the cross-sectional area and material geometry. The effects of loading on the second moment of inertia with respect to the medio-lateral ($I_{M\text{-}L}$) and cranio-caudal ($I_{C\text{-}C}$) axes are different. There was no significant difference in $I_{M\text{-}L}$ between the CTL and loaded groups at 3–13 N (Fig. 4b). However, $I_{C\text{-}C}$ in the loaded bone increased significantly from loads of 5–13 N, and the 3 N loading had no significant effect (Fig. 4c). The relative ratio of the second moment of inertia in the artificially loaded group to the CTL group is represented in Fig. 5. The ratio of increase in $I_{C\text{-}C}$ exhibited a load magnitude dependence ($p < 0.001$ by one-way ANOVA) corresponding with that of bone addition, reaching approximately 2.5-fold over the CTL bone in the 13 N-loaded group. Namely, the 1.3-fold increase in bone area produced a 2.5-fold increase in $I_{C\text{-}C}$.

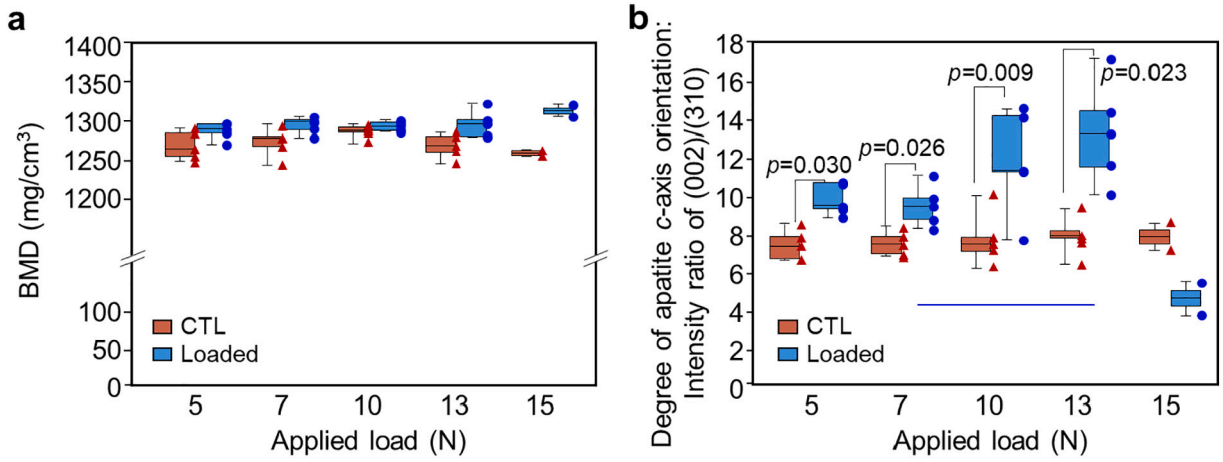

Fig. 6. Effects of artificial loading on the material properties of the newly formed bone. Comparison of (a) BMD and (b) degree of apatite *c*-axis orientation along the ulnar long axis. Data are displayed in a box-and-whisker diagram. The horizontal bar indicates significant differences in Tukey's HSD test. $n = 5$ for 5–13 N, and $n = 2$ for 15 N.

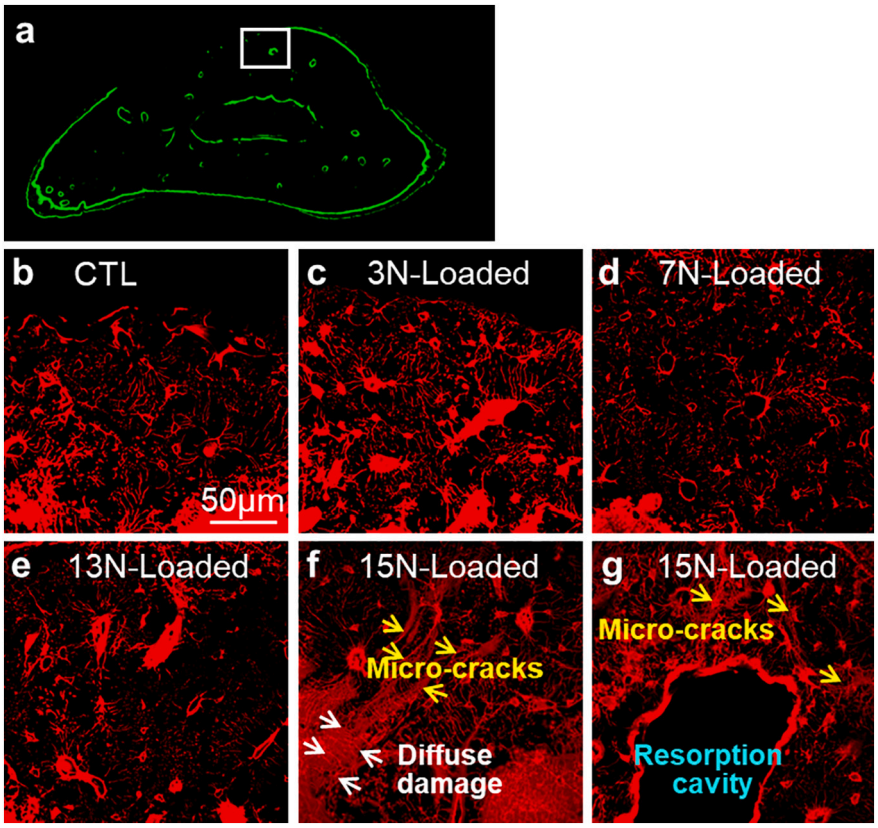

Fig. 7. Confocal images of basic fuchsin-stained transverse sections in medial surface (indicated by the white rectangle in a) at Point 6. In the 15 N-loaded bone, the microcracks (indicated by the yellow arrows in f and g), microdamage (indicated by the white arrows in f), and resorption cavity (shown in g) induced by loading are clearly seen. (For interpretation of the references to colour in this figure legend, the reader is referred to the web version of this article.)

3.4. Effect of load magnitude on bone material properties

The BMD after eight weeks of loading is shown in Fig. 6a. No significant increase was observed in the loaded bone compared to the CTL group. Furthermore, no load-magnitude dependence was observed ($p = 0.69$, one-way ANOVA).

Fig. 6b shows the degree of preferential apatite *c*-axis orientation, calculated as the relative intensity ratio of the (002) diffraction peak to the (310) peak. A significant increase was observed in the bones loaded at 5–13 N compared to that in the CTL group; the ratio was 1.6 times higher at 13 N loading. Further, the apatite orientation was significantly higher in the 13 N-loaded bone than in the 7 N-loaded bone ($p = 0.046$ in Tukey's HSD test).

3.5. Microdamage induced by axial compressive loading

Fuchsin staining of transverse sections of the ulnar medial surface is shown in Fig. 7. Bone matrix microcracks or microdamage were

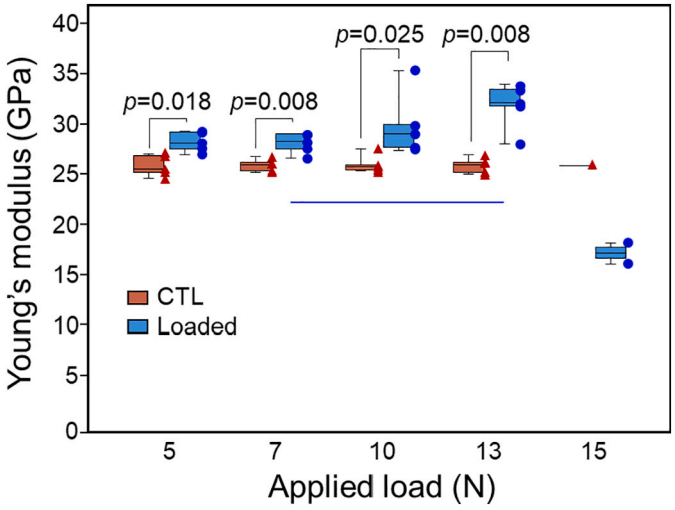

Fig. 8. Comparison of Young's modulus along the ulnar long axis of newly formed bone at Point 6. Data are displayed in a box-and-whisker diagram. The horizontal bar indicates significant differences in Tukey's HSD test. $n = 5$ for 5–13 N and $n = 2$ for 15 N.

observed only in the 15 N-loaded bone. Microdamage presented as ultrastructural matrix damage, as evident in the patches of diffuse basic fuchsin staining within the cortex and linearly stained microcracks (Fig. 7f, g). Microcracks (yellow arrow) or diffuse damage (white arrow) occurred principally on the ulnar medial surface, and a resorption cavity was also observed (Fig. 7g).

3.6. Effect of load magnitude on bone mechanical properties

The association between Young's modulus and peak load is presented in Fig. 8. The Young's modulus of the new bone was higher than that of the CTL, and a dose-response trend of the Young's modulus was observed in the 5–13 N groups. In bones loaded with 13 N, Young's modulus showed a maximum of about 32 GPa, 1.2 times that of the CTL group.

3.7. Contribution of BMD and apatite orientation to Young's modulus

Fig. 9 shows correlations between Young's modulus and BMD, or the degree of apatite *c*-axis orientation. We found that Young's modulus was significantly correlated with the apatite orientation (Fig. 9b), with a higher r^2 of 0.80. In contrast, the r^2 for the correlation between Young's modulus and BMD was quite lower, although the correlation was statistically significant (Fig. 9a). Based on a multiple linear regression analysis, Young's modulus can be expressed as a function of the BMD and apatite *c*-axis orientation as follows:

$$\text{Young's modulus} = 11.3 + 0.007\ (\text{BMD}) + 0.87\ (\text{apatite } c\text{-axis orientation}) \quad (1)$$

The statistics derived by multiple regression analysis are summarized in Table 1. The adjusted r^2 for this multiple regression was 0.80 with $p < 0.001$. The multiple regression coefficients (β) and *p*-values for the BMD and apatite *c*-axis orientation were (0.05, 0.51) and (0.87, < 0.001), respectively, indicating that the degree of apatite *c*-axis orientation contributes more to the variation in Young's modulus than it does the BMD.

4. Discussion

The formation of strong bones specific to the loaded direction should be an efficient mode of functional adaptation to mechanical environments. We used an *in vivo* artificial loading model of the rat ulna that can produce uniaxial compressive strain on the bone surface along the ulnar longitudinal axis. Because of the inherent curvature of the ulna, bending and compression are induced by *in vivo* artificial loading [19]. Bending is converted to axial stress in the longitudinal direction; therefore, the bone is loaded with the axial strain from bending and compression. The magnitude of the peak load (strain) is believed to affect bone mass and architecture [17]. The results of this study support those of previously reported experiments that used the same loading model, demonstrating that compressive axial strain superimposed on normal activity engenders an adaptive change in bone structural properties [17,19,21].

In this study, load magnitude-dependent changes were observed in

Table 1
Summary of the statistical outcomes of the multiple regression analysis expressed in Eq. (1).

Regression		Contribution to Young's modulus			
		BMD		Apatite orientation	
r^2	*p*	β	*p*	β	*p*
0.80	< 0.001	0.05	0.51	0.87	< 0.001

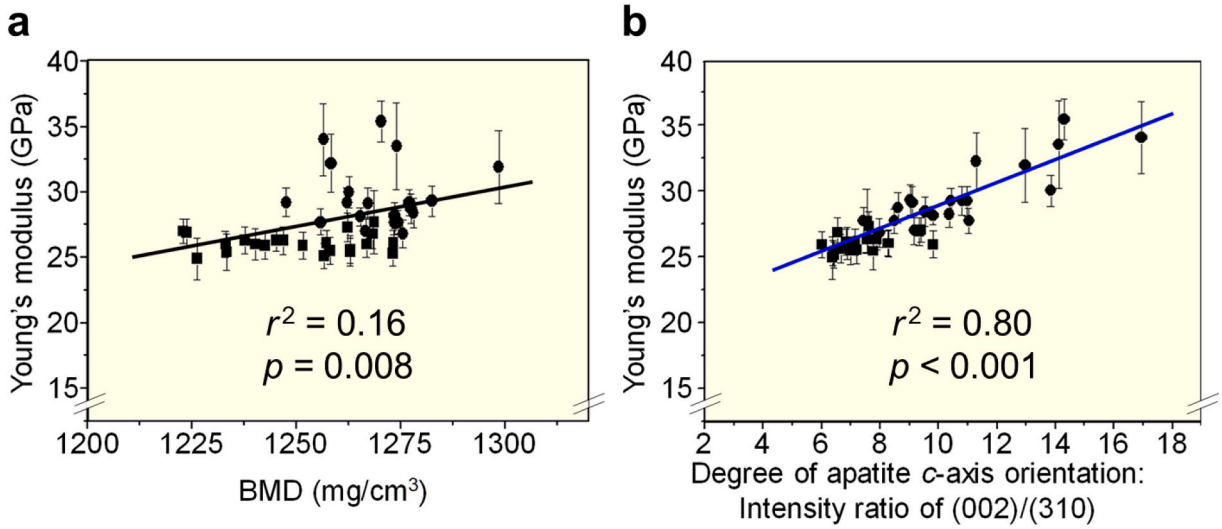

Fig. 9. Relationship between bone material properties and Young's modulus. Correlation of (a) BMD and (b) degree of apatite *c*-axis orientation with Young's modulus along the ulnar long axis. The r^2 and *p* values for each correlation (single regression) are presented together.

bone apposition and in the related changes in the ulnar cross-sectional area and second moment of inertia under artificial loading. Calcein labeling patterns suggestive of bone resorption were observed in the 3 N-loaded and CTL bones. This indicates growth-related drift from medial to lateral in the mid-diaphysis, presumably establishing the medial-to-lateral curvature of the bone [13]. Bone apposition at the medial periosteum occurred in the bones loaded to 5–13 N, and the cortical bone area increased. These results indicate that the minimum effective load magnitude was 5 N, corresponding to a 947 ± 162 με strain. This agrees well with the existing literature, as previous studies reported that the minimum effective strain for load-driven bone adaptation was approximately 1000 με [19,28].

The observed preferential bone apposition to the medial surface dramatically increased only $I_{C\text{-}C}$, while $I_{M\text{-}L}$ remained relatively constant. Bone apposition to the medial surface had little effect on $I_{M\text{-}L}$ because the bone apposition site was located on the medio-lateral axis. This asymmetrical change in the second moment of inertia suggests that *in vivo* compressive loading on the ulna causes bending where the neutral plane is defined as the plane containing the cranio-caudal and bone longitudinal axes. Previously characterized strain patterns at the diaphysis during external loading have shown that bending occurs in the medio-lateral direction owing to the natural curvature of the ulnar diaphysis [13]. By preferentially adding bone to the surface where the bending stress is greatest, bone can improve its resistance to mechanical stimuli in a geometrically efficient manner.

Such *in vivo* strain (load)-dependent changes in bone mass would be the general perception of functional adaptation in long bones to date. On the other hand, there is limited knowledge regarding the change in material properties (and thus quality) of bone under elevated loads. Therefore, in this study, we investigated the volumetric BMD and preferential apatite orientation as material features of bone. Many studies have reported that BMD measured using dual-energy X-ray absorptiometry (DXA) increases owing to exercise. However, DXA-measured BMD is area-based and reflects increased bone mass, while the volumetric BMD analyzed in this study reflects bone material density. We found that the volumetric BMD values of the newly formed bones in the loaded groups were not significantly higher than those in the CTL group. Similar bone adaptive changes with exercise have been reported in the human humerus, with the associated study concluding that exercise-induced bone gain is not due to volumetric BMD but to bone size [29]. In our study, the magnitude of the load had no significant effect on the volumetric BMD, indicating that the volumetric BMD was not sensitive to load. This differed from the response of the bone structural properties (*e.g.*, cross-sectional area and second moment of inertia), which tended to increase with the load magnitude.

Another important aspect of this study related to the material properties of bone was the preferential orientation of the apatite *c*-axis as the bone quality parameter, which is an essential contributor to the mechanical function of bone [11]. This study is the first of its kind to address the relationship between the load magnitude and apatite *c*-axis orientation. BMD showed no load magnitude dependence, whereas the enhancement in apatite orientation along the long bone axis tended to be dependent on load magnitude. The apatite orientation can thus be said to vary more significantly than BMD under elevated load and, moreover, to do so somewhat more sensitively than BMD with respect to the change in load magnitude. Functional adaptation by apatite orientation changes in rat ulna was found to have an adaptive window, including a strain range of at least 947 (5 N) to 2708 (13 N) με. On the other hand, peak loads of 15 N resulted in the formation of a woven bone exhibiting a less organized microstructure; hence, the corresponding strain of 3200 με might be outside the adaptive window. However, although apatite orientation tended to increase with the magnitude of the applied load (and thus strain), it is unclear whether this increase truly correlates to the load (strain) magnitude. This is because, as mentioned below, strain varies dynamically with changes in cross-sectional area and second moment of inertia, even when bone is exposed to loads of the same intensity. To accurately estimate the strain magnitude-dependency of apatite orientation increase, it is necessary to repeat the acquisition of bone geometry and analysis of strain using finite element calculations and to control the magnitude of strain at the bone surface to a constant value by adjusting the loading magnitude, which requires further research.

Accordingly, the mechanism by which mechanical loading influences the apatite *c*-axis orientation remains unclear. Takano et al. [30] and Turner et al. [31] have suggested that functional loading (below the magnitude of physiological loading) may influence the orientation of collagen fibers, which serve as a template for apatite precipitation and crystals. Paterson et al. [32] used non-hydrostatic thermodynamics to predict that tissue strain influences the crystal growth of inorganic minerals in a direction parallel to the principal strain. However, since recent studies have shown that apatite *c*-axis orientation in the direction of the principal strain does not increase in the absence of osteocalcin *in vivo*, even in mice undergoing normal activity [25], it appears that the non-hydrostatic thermodynamics of crystal growth cannot explain the increase in apatite orientation.

Alternatively, osteocytes may be involved in functional adaptation related to the change in apatite orientation. Osteocytes are well known as the major responsive cells in functional adaptation due to mechanical stimulation [33,34]. The response of osteocytes to mechanical stimuli has been extensively investigated in terms of their lacunar-canalicular network architecture, expression of biochemical factors, and, thus, osteogenic and resorptive activities. We have previously reported that the elongation (aspect ratio) and alignment of osteocyte lacunae to the long bone axis show a significant positive correlation with the degree of apatite orientation [35]. Kerschnitzki et al. [36] have also reported that the direction of the mineral particle (parallel to the crystallographic *c*-axis) alignment is always parallel to the osteocyte lacunar long axis, perpendicular to the direction of the canalicular alignment. The more the osteocyte lacunae are elongated with their major axis parallel to the long axis of the bone, the more the canaliculi are aligned perpendicularly to the long axis of the bone [35]. Therefore, it is possible that the more the osteocyte lacunae are elongated parallel to the long axis of the bone, the more the apatite orientation along the long axis of the bone increases. Grünewald et al. [37] investigated various properties of apatite minerals as a function of distance from the osteocyte lacuna. They reported a slight but significant distance dependence on mineral properties, including mineral orientation, which indicates that osteocytes are involved in the formation of mineral orientation.

The BMD generally accounts for a substantial proportion of the mechanical function of a bone and is strongly correlated with its mechanical performance. However, certain evidence suggests that an increased BMD does not necessarily lead to stronger bones; for instance, the BMD and bone strength are dissociated under conditions such as osteopetrosis [24,38] and fluorosis [39]. Bone strength depends not only on bone mass but also on the material properties of the bone tissue and its spatial arrangement. Therefore, bone quality should be considered when assessing the mechanical properties of bone. The apatite *c*-axis orientation, as a measure of bone quality, is an essential contributor to its mechanical functions. Apatite orientation would be an important factor in studies of bone mechanobiology and mechanical stimuli-related bone disorders.

Regarding the cancellous bone, apatite orientation also plays an important mechanical role. It is well documented that cancellous bone adaptively changes its trabecular strut structural anisotropy along stress lines [40]. In addition, inside a single trabecula, the apatite is preferentially oriented parallel to the trabecular beam direction [41], *i.e.*, the direction of applied stress [40]. In other words, the cancellous bone is strengthened by a hierarchical anisotropic structure: anisotropy of the trabecular strut structure and crystalline orientation within the trabecula. Although adaptive changes in cancellous bone are not the focus of this study, its analysis may reveal the nature of functional adaptation of bones, such as competing changes between the trabecular structure and

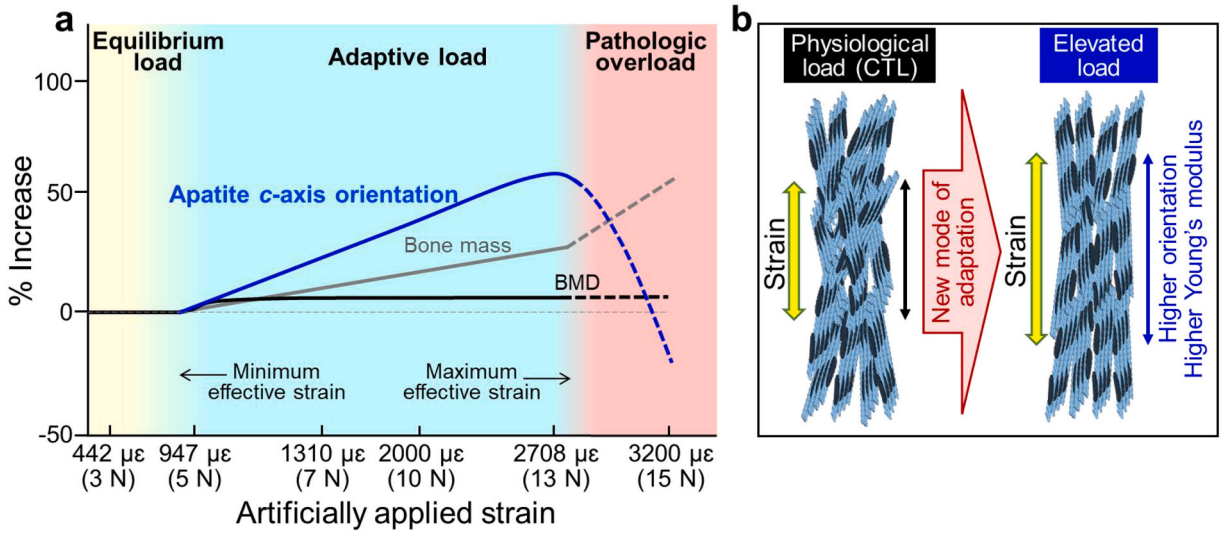

Fig. 10. (a) Schematic of the adaptive response of bone *via* bone mass, BMD, and degree of apatite *c*-axis orientation along the ulnar long axis, and (b) schematic comparison for microstructure between bones under physiological load (CTL) and elevated load. Under the elevated load (strain), the degree of apatite orientation along the strain direction increased, resulting in an increase in Young's modulus in the same direction, which was found to be a new mode of bone functional adaptation.

crystalline orientation in response to elevated mechanical stimuli and their contribution to enhancing trabecular bone strength, such as Young's modulus.

Finally, some limitations of this study should be mentioned. First, this study analyzed the adaptive response as average information within a region with ~100 μm length scale encompassing the lamellar structure. This study did not capture structural changes at scales below that which influence the mechanical properties of bones. For example, the twisted plywood structure, which was not captured in the scale of analysis in this study, contributes to crack propagation inhibition and, thus, energy absorptivity [42]. Future work is expected to elucidate the adaptive responses occurring at smaller scale lengths than analyzed in this study and their contribution to the mechanical properties. Secondly, it is necessary to clarify the effect of changes occurring in the newly formed bone on the overall bone strength, *e.g.*, the bending modulus and strength of the whole bone. Third, and related to the second limitation, the magnitude and distribution of generated strain by artificial loading should be dynamically changed owing to adaptive changes occurring on bone during the test period, which was not considered.

5. Conclusions

Using an *in vivo* rat ulnar loading model, we elucidated that quantitative changes in the bone mass, as previously established, and changes in bone quality determined by the bone apatite orientation are involved in the functional adaptation of the bone. The apatite *c*-axis oriented more in the direction of the principal strain in a strain magnitude-dependent manner (Fig. 10), and Young's modulus in the same direction increased correspondingly with the degree of apatite orientation. However, there was no strain magnitude dependence in the BMD. The change in apatite orientation is a very efficient and reasonable mode of functional adaptation that can strengthen bones, specifically in the loading direction. The discovery of this new mode of functional adaptation will provide new insights into the biomechanical performance of bones, the formation of anisotropic bone material, and the development of orthopedic and dental implants to recover bone functionality.

CRediT authorship contribution statement

Jun Wang: Writing – original draft, Visualization, Methodology, Investigation, Formal analysis. **Takuya Ishimoto:** Writing – review & editing, Supervision, Methodology, Formal analysis. **Tadaaki Matsuzaka:** Writing – review & editing, Visualization. **Aira Matsugaki:** Supervision, Methodology. **Ryosuke Ozasa:** Methodology, Investigation. **Takuya Matsumoto:** Supervision, Funding acquisition. **Mikako Hayashi:** Supervision, Investigation. **Hyoung Seop Kim:** Supervision, Investigation. **Takayoshi Nakano:** Writing – review & editing, Supervision, Project administration, Funding acquisition, Conceptualization.

Declaration of competing interest

None.

Data availability

Data will be made available on request.

Acknowledgments

This work was supported by a Grant-in-Aid for Scientific Research (Grant Number: JP23H00235) from the Japan Society for the Promotion of Science (JSPS). This work was also partly supported by CREST (Grant Numbers: JPMJCR2194 and JPMJCR22L5) from the Japan Science and Technology Agency (JST).

Appendix A. Supplementary data

Supplementary data to this article can be found online at https://doi.org/10.1016/j.bone.2024.117024.

References

[1] T.C. Lee, D. Taylor, Bone remodelling: should we cry Wolff? Ir. J. Med. Sci. 168 (1999) 102–105, https://doi.org/10.1007/BF02946474.
[2] C.T. Rubin, L.E. Lanyon, Regulation of bone mass by mechanical strain magnitude, Calcif. Tissue Int. 37 (1985) 411–417, https://doi.org/10.1007/BF02553711.
[3] H.M. Frost, Bone, 'mass' and the "mechanostat": a proposal, Anat. Rec. 219 (1987) 1–9, https://doi.org/10.1002/ar.1092190104.
[4] B. Viswanath, R. Raghavan, U. Ramamurty, N. Ravishankar, Mechanical properties and anisotropy in hydroxyapatite single crystals, Scr. Mater. 57 (2007) 361–364, https://doi.org/10.1016/j.scriptamat.2007.04.027.
[5] Y. Tanaka, A. Kubota, M. Matsusaki, T. Duncan, Y. Hatakeyama, K. Fukuyama, A. J. Quantock, M. Yamato, M. Akashi, K. Nishida, Anisotropic mechanical properties of collagen hydrogels induced by uniaxial-flow for ocular applications, J. Biomater.

Sci. Polym. Ed. 22 (2011) 1427–1442, https://doi.org/10.1163/092050610X510542.
[6] S. Li, E. Demirci, V.V. Silberschmidt, Variability and anisotropy of mechanical behavior of cortical bone in tension and compression, J. Mech. Behav. Biomed. Mater. 21 (2013) 109–120, https://doi.org/10.1016/j.jmbbm.2013.02.021.
[7] S. Jia, J. Li, X. Hu, X. Wu, H. Gong, Improved fatigue properties, bone microstructure and blood glucose in type 2 diabetic rats with verapamil treatment, Clin. Biomech. 98 (2022) 105719, https://doi.org/10.1016/j.clinbiomech.2022.105719.
[8] Y. Shinno, T. Ishimoto, M. Saito, R. Uemura, M. Arino, K. Marumo, T. Nakano, M. Hayashi, Comprehensive analyses of how tubule occlusion and advanced glycation end-products diminish strength of aged dentin, Sci. Rep. 6 (2016) 19849, https://doi.org/10.1038/srep19849.
[9] H. Peterlik, P. Roschger, K. Klaushofer, P. Fratzl, From brittle to ductile fracture of bone, Nat. Mater. 5 (2006) 52–55, https://doi.org/10.1038/nmat1545.
[10] D.J. Buss, R. Kröger, M.D. McKee, N. Reznikov, Hierarchical organization of bone in three dimensions: a twist of twists, J. Struct. Biol. X. 6 (2022) 100057, https://doi.org/10.1016/j.yjsbx.2021.100057.
[11] T. Ishimoto, T. Nakano, Y. Umakoshi, M. Yamamoto, Y. Tabata, Degree of biological apatite c-axis orientation rather than bone mineral density controls mechanical function in bone regenerated using recombinant bone morphogenetic protein-2, J. Bone Miner. Res. 28 (2013) 1170–1179, https://doi.org/10.1002/jbmr.1825.
[12] T. Nakano, K. Kaibara, Y. Tabata, N. Nagata, S. Enomoto, E. Marukawa, Y. Umakoshi, Unique alignment and texture of biological apatite crystallites in typical calcified tissues analyzed by microbeam X-ray diffractometer system, Bone 31 (2002) 479–487, https://doi.org/10.1016/S8756-3282(02)00850-5.
[13] A.G. Torrance, J.R. Mosley, R.F. Suswillo, L.E. Lanyon, Noninvasive loading of the rat ulna in vivo induces a strain-related modeling response uncomplicated by trauma or periostal pressure, Calcif. Tissue Int. 54 (1994) 241–247, https://doi.org/10.1007/BF00301686.
[14] A. Morse, F.C. Ko, M.M. McDonald, L.R. Lee, A. Schindeler, M.C.H. van der Meulen, D.G. Little, Increased anabolic bone response in Dkk1 KO mice following tibial compressive loading, Bone 131 (2020) 115054, https://doi.org/10.1016/j.bone.2019.115054.
[15] X. Zhang, X. Liu, Z. Yan, J. Cai, F. Kang, S. Shan, P. Wang, M. Zhai, X.E. Edward Guo, E. Luo, D. Jing, Spatiotemporal characterization of microdamage accumulation in rat ulnae in response to uniaxial compressive fatigue loading, Bone 108 (2018) 156–164, https://doi.org/10.1016/j.bone.2018.01.011.
[16] A. Raman, Appositional growth rate in rat bones using the tetracycline labelling method, Acta Orthop. Scand. 40 (1969) 193–197, https://doi.org/10.3109/17453676908989498.
[17] J.R. Mosley, B.M. March, J. Lynch, L.E. Lanyon, Strain magnitude related changes in whole bone architecture in growing rats, Bone 20 (1997) 191–198, https://doi.org/10.1016/S8756-3282(96)00385-7.
[18] K.J. Lewis, D. Frikha-Benayed, J. Louie, S. Stephen, D.C. Spray, M.M. Thi, Z. Seref-Ferlengez, R.J. Majeska, Sh. Weinbaum, M.B. Schaffler, Osteocyte calcium signals encode strain magnitude and loading frequency in vivo, Proc. Natl. Acad. Sci. U. S. A. 114 (2017) 11775–11780, https://doi.org/10.1073/pnas.1707863114.
[19] Y.F. Hsieh, A.G. Robling, W.T. Ambrosius, D.B. Burr, C.H. Turner, Mechanical loading of diaphyseal bone in vivo: the strain threshold for an osteogenic response varies with location, J. Bone Miner. Res. 16 (2001) 2291–2297, https://doi.org/10.1359/jbmr.2001.16.12.2291.
[20] Q.A. Meslier, N. DiMauro, P. Somanchi, S. Nano, S.J. Shefelbine, Manipulating load-induced fluid flow in vivo to promote bone adaptation, Bone 165 (2022) 116547, https://doi.org/10.1016/j.bone.2022.116547.
[21] Y. Lu, G. Thiagarajan, D.P. Nicolella, M.L. Johnson, Load/strain distribution between ulna and radius in the mouse forearm compression loading model, Med. Eng. Phys. 34 (2012) 350–356, https://doi.org/10.1016/j.medengphy.2011.07.022.
[22] D.B. Burr, M. Hooser, Alterations to the en bloc basic fuchsin staining protocol for the demonstration of microdamage produced in vivo, Bone 17 (1995) 431–433, https://doi.org/10.1016/s8756-3282(95)00241-3.
[23] R. Ozasa, M. Saito, T. Ishimoto, A. Matsugaki, Y. Matsumoto, T. Nakano, Combination treatment with ibandronate and eldecalcitol prevents osteoporotic bone loss and deterioration of bone quality characterized by nano-arrangement of the collagen/apatite in an ovariectomized aged rat model, Bone 157 (2022) 116309, https://doi.org/10.1016/j.bone.2021.116309.
[24] T. Ishimoto, B. Sato, J.W. Lee, T. Nakano, Co-deteriorations of anisotropic extracellular matrix arrangement and intrinsic mechanical property in c-src deficient osteopetrotic mouse femur, Bone 103 (2017) 216–223, https://doi.org/10.1016/j.bone.2017.06.023.
[25] T. Moriishi, R. Ozasa, T. Ishimoto, T. Nakano, T. Hasegawa, T. Miyazaki, W. Liu, R. Fukuyama, Y. Wang, H. Komori, X. Qin, N. Amizuka, T. Komori, Osteocalcin is necessary for the alignment of apatite crystallites, but not glucose metabolism, testosterone synthesis, or muscle mass, PLoS Genet. 16 (2020) e1008586, https://doi.org/10.1371/journal.pgen.1008586.
[26] T. Ishimoto, T. Nakano, M. Yamamoto, Y. Tabata, Biomechanical evaluation of regenerating long bone by nanoindentation, J. Mater. Sci. Mater. Med. 22 (2011) 969–976, https://doi.org/10.1007/s10856-011-4266-y.
[27] W.C. Oliver, G.M. Pharr, An improved technique for determining hardness and elastic modulus using load and displacement sensing indentation experiments, J. Mater. Res. 7 (1992) 1564–1583, https://doi.org/10.1557/JMR.1992.1564.
[28] L.B. Meakin, G.L. Galea, T. Sugiyama, L.E. Lanyon, J.S. Price, Age-related impairment of bones' adaptive response to loading in mice is associated with sex-related deficiencies in osteoblasts but no change in osteocytes, J. Bone Miner. Res. 29 (2014) 1859–1871, https://doi.org/10.1002/jbmr.2222.
[29] H. Haapasalo, S. Kontulainen, H. Sievänen, P. Kannus, M. Järvinen, I. Vuori, Exercise-induced bone gain is due to enlargement in bone size without a change in volumetric bone density: a peripheral quantitative computed tomography study of the upper arms of male tennis players, Bone 27 (2000) 351–357, https://doi.org/10.1016/S8756-3282(00)00331-8.
[30] Y. Takano, C.H. Turner, I. Owan, R.B. Martin, S.T. Lau, M.R. Forwood, D.B. Burr, Elastic anisotropy and collagen orientation of osteonal bone are dependent on the mechanical strain distribution, J. Orthop. Res. 17 (1999) 59–66, https://doi.org/10.1002/jor.1100170110.
[31] C.H. Turner, A. Chandran, R.M.V. Pidaparti, The anisotropy of osteonal bone and its ultrastructural implications, Bone 17 (1995) 85–89, https://doi.org/10.1016/8756-3282(95)00148-7.
[32] M.S. Paterson, Nonhydrostatic thermodynamics and its geologic applications, Rev. Geophys. 11 (1973) 355–389, https://doi.org/10.1029/RG011i002p00355.
[33] Y. Moharrer, J.D. Boerckel, Tunnels in the rock: dynamics of osteocyte morphogenesis, Bone 153 (2021) 116104, https://doi.org/10.1016/j.bone.2021.116104.
[34] W. Sang, A. Ural, Influence of osteocyte lacunar-canalicular morphology and network architecture on osteocyte mechanosensitivity, Curr. Osteoporos. Rep. 21 (2023) 401–413, https://doi.org/10.1007/s11914-023-00792-9.
[35] T. Ishimoto, K. Kawahara, A. Matsugaki, H. Kamioka, T. Nakano, Quantitative evaluation of osteocyte morphology and bone anisotropic extracellular matrix in rat femur, Calcif. Tissue Int. 109 (2021) 434–444, https://doi.org/10.1007/s00223-021-00852-1.
[36] M. Kerschnitzki, P. Kollmannsberger, M. Burghammer, G.N. Duda, R. Weinkamer, W. Wagermaier, P. Fratzl, Architecture of the osteocyte network correlates with bone material quality, J. Bone Miner. Res. 28 (2013) 1837–1845, https://doi.org/10.1002/jbmr.1927.
[37] T.A. Grünewald, A. Johannes, N.K. Wittig, J. Palle, A. Rack, M. Burghammer, H. Birkedal, Bone mineral properties and 3D orientation of human lamellar bone around cement lines and the Haversian system, IUCrJ 10 (2023) 189–198, https://doi.org/10.1107/S2052252523000866.
[38] A.K. Nepal, H.W. van Essen, A.J. van der Veen, W.N. van Wieringen, A.W. D. Stavenuiter, F.K. Cayami, G. Pals, D. Micha, D. Vanderschueren, P. Lips, N. Bravenboer, Mechanical stress regulates bone regulatory gene expression independent of estrogen and vitamin D deficiency in rats, J. Orthop. Res. 39 (2021) 42–52, https://doi.org/10.1002/jor.24775.
[39] C.H. Turner, L.P. Garetto, A.J. Dunipace, W. Zhang, M.E. Wilson, M.D. Grynpas, D. Chachra, R. McClintock, M. Peacock, G.K. Stookey, Fluoride treatment increased serum IGF-1, bone turnover, and bone mass, but not bone strength, in rabbits, Calcif. Tissue Int. 61 (1997) 77–83, https://doi.org/10.1007/s002239900299.
[40] T.L. Kivell, A review of trabecular bone functional adaptation: what have we learned from trabecular analyses in extant hominoids and what can we apply to fossils? J. Anat. 228 (2016) 569–594, https://doi.org/10.1111/joa.12446.
[41] T. Ishimoto, K. Yamada, H. Takahashi, M. Takahata, M. Ito, T. Hanawa, T. Nakano, Trabecular health of vertebrae based on anisotropy in trabecular architecture and collagen/apatite micro-arrangement after implantation of intervertebral fusion cages in the sheep spine, Bone 108 (2018) 25–33, https://doi.org/10.1016/j.bone.2017.12.012.
[42] F.D. Fischer, O. Kolednik, J. Predan, H. Razi, P. Fratzl, Crack driving force in twisted plywood structures, Acta Biomater. 55 (2017) 349–359, https://doi.org/10.1016/j.actbio.2017.04.007.